

# Eulerian-Lagrangian Simulation of a Turbulent Evaporating Spray using RANS Modeling

**Rodrigo B. Piccinini**  
**Marcelo J.S. de Lemos\***

*Departamento de Energia - IEME*  
*Instituto Tecnológico de Aeronáutica - ITA*  
*12228-900 - São José dos Campos - SP, Brazil*  
**\*Corresponding author** E-mail: [delemos@ita.br](mailto:delemos@ita.br)

---

## Abstract

RANS simulation is applied to a turbulent and evaporating spray of acetone in an air co-flow stream. The air is a continuous phase in an Eulerian description and the liquid is a dispersed phase of point-particles in a Lagrangian description. An approximation of zero Mach number was applied to the governing equations of the continuous phase. Turbulence was modeled using k-epsilon model. Submodels were used for heat and mass inter-phase transfers and Nusselt and Sherwood numbers are given by empirical correlations for convective droplet heating and evaporation. The spray interaction with turbulence is only accounted for in droplet motion using the random walk procedure. The numerical results were compared to measurements and a reasonable prediction was found for droplet and gas velocities and liquid evaporation, although underestimated.

## *Keywords:*

spray, round jet, low Mach number, lagrangian, point-particle method

---

## Nomenclature:

$C_D$	droplet drag coefficient
$c_p$	specific heat at constant pressure [ $J/kg/K$ ]
$D$	droplet diameter [ $m$ ]
$\tilde{f}$	favre-average of function $f$
$f''$	deviation of favre-averaged function $\tilde{f}$
$\bar{f}$	time-average of function $f$
$f'$	deviation of time-averaged function $\bar{f}$
$\mathbf{g}$	vector field of gravity force [ $m/s^2$ ]
$\dot{m}_d$	mass flow rate of liquid injection [ $kg/s$ ]
$\dot{m}_g$	gas mass rate [ $kg/s$ ]
$\dot{m}_{vapor}$	acetone vapor mass rate [ $kg/s$ ]
$h_d$	droplet enthalpy [ $J/kg$ ]
$h_s$	gas sensible enthalpy [ $J/kg$ ]
$k$	turbulent kinetic energy [ $J/kg$ ]
$\hat{k}$	jet dimensionless $k$ : $\hat{k} = k/(\tilde{U}_{x,0} - \tilde{U}_{cl})^2$
$L_v$	latent heat of vaporization [ $J/kg$ ]
$m_d$	droplet mass [ $kg$ ]
$M$	Mach number
$p_0$	thermodynamic pressure [ $Pa$ ]
$p_2$	dynamic pressure [ $Pa$ ]
$p$	pressure [ $Pa$ ]
$Pr$	Prandtl number

$Re_d$	droplet Reynolds number, $Re = (\rho \mathbf{U} _{slip}D)/\mu$
$S_{hs}$	spray enthalpy source term [ $J/m^3/s$ ]
$S_m$	spray mass source term [ $kg/m^3/s$ ]
$S_{mom}$	spray momentum source term [ $kg/m^3/s$ ]
$S_{Y_k}$	spray source term of species k [ $kg/m^3/s$ ]
$Sc$	Schmidt number
$Sh$	Sherwood number
$T_d$	droplet temperature [ $K$ ]
$T$	gas temperature [ $K$ ]
$t$	time [ $s$ ]
$\mathbf{U}$	gas velocity vector [ $m/s$ ]
$\mathbf{U}_d$	droplet velocity vector [ $m/s$ ]
$\mathbf{U}_{slip}$	droplet velocity relative to the gas: $\mathbf{U}_{slip} = \mathbf{U}_d - \mathbf{U}$ [ $m/s$ ]
$\tilde{U}_{x,0}$	jet centerline velocity
$\tilde{U}_{x,cf}$	co-flow velocity
$\hat{U}$	dimensionless jet velocity, $\hat{U} = (\tilde{U}_x - \tilde{U}_{x,cf})/(\tilde{U}_{x0} - \tilde{U}_{x,cf})$
$y_{1/2}(x)$	jet half-radius, the radial coordinate for which $\tilde{U}_x(y = y_{1/2}) = 1/2\tilde{U}_{x,0}$
$\hat{y}(x, y)$	dimensionless radial coordinate: $\hat{y}(x, y) = y/y_{1/2}$
$x$	axial coordinate [ $m$ ]
$\mathbf{x}$	position vector [ $m$ ]
$y$	radial coordinate [ $m$ ]
$Y_k$	mass fraction of species k
$W_k$	molecular weight of species k [ $kg/mol$ ]

**Greek Characters:**

$\alpha$	thermal diffusivity [ $m^2/s$ ]
$\gamma$	ratio of constant pressure and constant volume specific heats
$\epsilon$	dissipation rate of turbulent kinetic energy [ $J/kg/s$ ]
$\kappa$	thermal conductivity [ $W/m/K$ ]
$\mu$	gas dynamic viscosity [ $Pa.s$ ]
$\nu$	gas kinematic viscosity [ $m^2/s$ ]
$\nu_T$	turbulent viscosity [ $m^2/s$ ]
$\hat{\nu}_T$	jet dimensionless turbulent viscosity: $\hat{\nu}_T = \mu/(\bar{\rho}\tilde{U}_{x,0}y_{1/2})$
$\rho$	gas density [ $kg/m^3$ ]
$\rho_d$	droplet density [ $kg/m^3$ ]
$\tau$	viscous stress tensor [ $Pa$ ]
$\tau_e$	droplet evaporation relaxation time [ $s$ ]
$\tau_h$	droplet heating relaxation time [ $s$ ]
$\tau_u$	droplet momentum relaxation time [ $s$ ]
$\phi_{v,l}$	liquid volume fraction

**Special Characters:**

cdf	cumulative density function
pdf	probability density function
pmf	probability mass function
SMD	Sauter mean diameter
$\mathcal{D}_k$	binary diffusion coefficient of species k [ $m^2/s$ ]

## 1. Introduction

A spray jet is a particular case of a dispersed multiphase flow originated by the instabilization of a liquid jet emerging in a gaseous atmosphere. The spray is composed by the continuous gaseous phase and the dispersed phase of liquid droplets. Depending on the liquid volumetric fraction, the spray may be classified as dense ( $\phi_l > 10^{-3}$ ) or dilute ( $\phi_l \leq 10^{-3}$ ). The dilute sprays are commonly modeled using the so called two-way coupling, where interaction between gas and liquid droplets is modeled, but interaction among droplets is neglected.

RANS modeling has been extensively used to spray jets simulations, see Baumgarten [6], and, more recently, large-eddy (LES) and direct simulations (DNS) have also been applied. Independently on the turbulence modeling, droplet heating and evaporation are often similarly modeled with empirical correlations for Nusselt and Sherwood numbers, such as those of Ranz and Marshall's Ranz and Marshall [27]. This indicates that much of the improvement obtained in LES simulations in the prediction of droplet velocity and evaporation rate, e.g. Bini and Jones [7] and Apte et al. [3], was due to the best modeling of turbulent motion and the allowance of gas properties such as temperature ( $T$ ) and species mass fractions ( $Y_k$ ) to deviate from mean values. It certainly provides a more accurate description of droplet environment in a turbulent spray jet. Actually, Bini and Jones [7] has also shown that subgrid modeling of Sherwood number in LES further improved predictions of droplet evaporation.

This scenario suggests the possibility of improving RANS simulations with stochastic submodeling of not only droplet dispersion, but of heat and

mass transfers as well. Also, the proposition of RANS submodels would certainly benefit from the results coming from LES and DNS.

This paper presents results of applying RANS modeling to the experiment developed by Chen et al. [9]. It has found overestimation of jet spread rate using the usual coefficients of k-epsilon model and underprediction of droplet velocity and evaporation rate, specially after the jet core. It suggests that future modification of turbulence model coefficients and stochastic submodels for heat and mass transfers could improve predictions.

## 2. Governing Equations

### 2.1. Continuous Phase

The equations for the continuous gaseous phase were derived from the fully compressible formulation, Poinso and Veynante [25], with additional spray source terms ( $S_m$ ,  $S_Y$ ,  $S_{mom}$  and  $S_{hs}$ ). It was applied the low Mach number approximation, see Majda and Sethian [20], and performed the Reynolds and Favre averages for turbulence modeling.

The low Mach number approximation expands all variables in power series of  $\xi = \sqrt{\gamma}M^2$  and only collects the equations of zeroth order in  $\xi$ . This procedure splits pressure in two parcels,

$$p = p_0(t) + p_2(\mathbf{x}, t)\xi^2 + O(\xi^3) . \quad (1)$$

$p_0$  is called the thermodynamic pressure, it is shown to be function of time only and it is present in the state and energy equations;  $p_1$  is not present in the equations for zeroth order terms and  $p_2$  is the dynamic pressure, whose gradient is present in the momentum equation.

The continuity equation reads:

$$\frac{\partial \bar{\rho}}{\partial t} + \nabla \cdot (\bar{\rho} \tilde{\mathbf{U}}) = \bar{S}_m. \quad (2)$$

The acetone ( $Y_{ac}$ ) conservation equation for binary diffusion and unitary Schmidt number reads:

$$\frac{\partial \bar{\rho} \tilde{Y}_{ac}}{\partial t} + \nabla \cdot (\bar{\rho} \tilde{\mathbf{U}} \tilde{Y}_{ac}) = \nabla \cdot [\bar{\rho} (\nu + \nu_T) \nabla \tilde{Y}_{ac}] + \bar{S}_{Y_{ac}}, \quad (3)$$

air is treated as an inert species with

$$\tilde{Y}_{air} = 1 - \tilde{Y}_{ac}. \quad (4)$$

The momentum equation reads:

$$\frac{\partial \bar{\rho} \tilde{\mathbf{U}}}{\partial t} + \nabla \cdot (\bar{\rho} \tilde{\mathbf{U}} \tilde{\mathbf{U}}) = -\nabla \bar{p}_2 + \nabla \cdot \bar{\boldsymbol{\tau}} + \bar{\rho} \mathbf{g} + \bar{\mathbf{S}}_{mom}. \quad (5)$$

where  $\tau$  is the viscous stress tensor with effective viscosity  $\mu_{eff} = \mu + \mu_T$ .

The energy equation is written in terms of sensible enthalpy with unitary turbulent Prandtl number:

$$\frac{\partial \bar{\rho} \tilde{h}_s}{\partial t} + \nabla \cdot (\bar{\rho} \tilde{\mathbf{U}} \tilde{h}_s) = \nabla \cdot \bar{\mathbf{J}}_s + \bar{S}_{h_s}, \quad (6)$$

where

$$\bar{\mathbf{J}}_s = \bar{\rho} (\alpha + \nu_T) \nabla \tilde{h}_s. \quad (7)$$

The pressure work ( $Dp/Dt$ ) and species thermal diffusion were neglected.

State Equation is:

$$\bar{p}_0 W = R \bar{\rho} \tilde{T} \quad (8)$$

The k-epsilon equations are those presented in Nordin [22] with  $\dot{W}^s = 0$ , that is, no sink of turbulent kinetic energy was defined here due to the work done by the eddies on the droplets. The model has six parameters whose values are shown in Table 2.

### 3. Dispersed Phase

The dispersed phase is written in a Lagrangian reference frame. The droplet equations are:

$$\text{Momentum: } \frac{d\mathbf{U}_d}{dt} = -\frac{\mathbf{U}_{slip}}{\tau_u} + \mathbf{g} \quad (9)$$

$$\text{Mass: } \frac{dm_d}{dt} = -\frac{m_d}{\tau_e}, \quad (10)$$

$$\text{Energy: } \frac{dT_d}{dt} = \frac{T - T_d}{\tau_h} f - \frac{1}{c_{p,d}} \frac{L_v(T_d)}{\tau_e} \quad (11)$$

In the momentum equation,  $\tau_u$  is the momentum relaxation time:

$$\tau_u = \frac{8m_d}{\pi\rho C_D D^2 |\mathbf{U}_{slip}|} = \frac{4}{3} \frac{\rho_d D}{\rho C_D |\mathbf{U}_{slip}|}. \quad (12)$$

The drag coefficient ( $C_D$ ) is computed using the expression in Nordin [22].

The droplet slip velocity is:

$$\mathbf{U}_{slip} = \mathbf{U}_d - \tilde{\mathbf{U}} - \mathbf{U}'', \quad (13)$$

where  $\tilde{\mathbf{U}}$  is the Favre-averaged gas velocity computed in Equation (5). The fluctuation of gas velocity ( $\mathbf{U}''$ ) is determined using the random walk procedure of O'Rourke [24]. For the k-epsilon model, a characteristic velocity may be defined as:

$$\langle U'' \rangle = \sqrt{\frac{2}{3}k}. \quad (14)$$

The magnitude of the velocity fluctuation ( $\mathbf{U}''$ ) is then sampled from a Gaussian distribution with a variance equal to  $\langle U'' \rangle$  and zero mean. Finally, the direction of  $\mathbf{U}''$  is randomly chosen.

The sampling is performed once the time passed from the last sampling is greater than the characteristic time  $\tau_{turb}$ : the minimum between the eddy



lifetime and the time taken to the droplet to cross it, given by the ratio of a turbulent length scale ( $l_t = C_\mu^{3/4} k^{3/2}/\epsilon$ ) and the magnitude of the droplet slip velocity:

$$\tau_{turb} = \min \left[ \frac{k}{\epsilon}, \frac{k^{3/2}}{\epsilon} \frac{C_\mu^{3/4}}{|\mathbf{U}_{slip}|} \right]. \quad (15)$$

The characteristic time scales for heating ( $\tau_h$ ) and evaporation ( $\tau_e$ ) are:

$$\tau_h = \frac{m_d c_{l,d}}{\pi D \kappa Nu}, \quad \tau_e = \frac{m_d}{\pi D D Sh \rho_v \ln \left( \frac{1-Y_{v,\infty}}{1-Y_{v,s}} \right)}. \quad (16)$$

The  $f$  factor in the energy equation corrects for the heat not transferred to the droplet, but to the surrounding vapor:

$$f = \frac{z}{e^z - 1} \quad \text{and} \quad z = -\frac{c_{p,f} \dot{m}_f B}{\pi D^2 h_c}. \quad (17)$$

The Nusselt and Sherwood numbers are computed from the empirical correlations of Ranz and Marshall [27]:

$$Nu = 2.0 + 0.6 Re^{1/2} Pr^{1/3}, \quad (18)$$

$$Sh = 2.0 + 0.6 Re^{1/2} Sc^{1/3}. \quad (19)$$

They account for the extra heat and mass transfer due to gas motion around the droplet. All gas properties in Equations (18) and (19) are computed using the film temperature, see Wakil et al. [32].

The vapor mass fraction in the droplet surrounding ( $Y_{v,s}$ ) is obtained assuming liquid-vapor equilibrium and using Raoult's law:

$$Y_{v,s} = \frac{p_v(T_d)}{p} \frac{W_v}{W}, \quad (20)$$

$p_v(T_d)$  is the equilibrium vapor pressure at droplet temperature  $T_d$ .

#### 4. The Experiment Configuration

Chen et al. [9] performed at Sydney University a detailed experimental investigation of a turbulent evaporating jet of acetone. Droplet diameter, droplet velocity, droplet number density and liquid volumetric flux were measured using a two-component phase Doppler interferometry (PDI) and acetone vapor mass flux was measured using planar laser-induced fluorescence (PLIF).

The experiment consists of a spray nozzle centered on the exit plane of a wind tunnel with 150mm by 150mm that supplies a co-flowing air stream, see Figure 1. Inside the nozzle, a pressurized liquid jet is surrounded by a carrier air flow until the nozzle exit. The co-flow has a low turbulence intensity of less than 2%, so that the effect on the spray jet turbulence is negligible. The main benefit of this setup is the avoidance of flow recirculation near the nozzle exit, simplifying the boundary conditions for a numerical simulation.

Table 1 summarizes the basic characteristics of the experiment. The droplet velocities in the nozzle exit were measured and the droplet and gas temperatures were calculated from thermal equilibrium assumption. The statistical distribution of droplet diameters in the nozzle was not provided by the experiment and only the Sauter mean diameter (SMD) is known. A lognormal distribution was then specified with expected value and standard deviation being, respectively,  $E = 10 \mu m$  and  $SD = 5.5 \mu m$ .

#### 5. Aspects of the Numerical Solution

The numerical solution of the equations in Section 2 was obtained using finite volume method with the OpenFOAM code, more specifically the die-

selfFOAM solver and dieselSpray library. Minor modifications were made in order to solve for the low Mach number equations and to adapt boundary conditions to the experiment.

### 5.1. Domain Discretization (The Numerical Grid)

Two axisymmetric (2D) orthogonal mesh grids were built: a fine and a coarse grid. OpenFOAM uses the collocated grid arrangement. The fine grid was composed of 14,800 cells (74 cells in the radial direction and 200 in the axial direction) and the coarse grid was composed of 5,460 cells (42 in the radial direction and 130 in the axial direction).

Solutions for both grids were obtained for a pure gas flow. In despite of some differences, the coarse grid solution was considered enough accurate and it was used for the results presented in this paper.

Droplets were injected in the domain at a rate of  $5 \times 10^5$  *droplets/s*.

### 5.2. Equation Discretization

The general transport equation for a scalar intensive property  $\phi$  is:

$$\underbrace{\frac{\partial \rho \phi}{\partial t}}_{\text{temporal derivative}} + \underbrace{\nabla \cdot (\rho \mathbf{U} \phi)}_{\text{advection}} - \underbrace{\nabla \cdot (\rho \Gamma \nabla \phi)}_{\text{diffusion}} = \underbrace{S(\phi)}_{\text{source}} \quad (21)$$

The discretization of each term used the following schemes:

- Temporal derivative: Euler implicit method;
- Advection term: Gauss theorem is applied to transform the divergence in surface integrals and the upwind scheme is used to interpolate values from cell center to cell faces;

- Diffusion term: Gauss theorem for the divergent with linear interpolation for the diffusion coefficient from cell center to cell faces. Central difference is used for the gradient;
- Sources: all sprays sources are explicitly handled. The spray is evolved from time step "n" to "n+1" using the gas phase properties at time step "n", and all source terms are computed. The gas is then evolved to time step "n+1".

After discretization, the resulting algebraic equations were solved in segregated linear systems using conjugate gradient algorithms. The pressure-velocity coupling is solved using the PISO algorithm, see Issa [14]. In the low Mach number formulation, the convective-diffusive pressure equation for compressible flows becomes a Poisson equation as it is for incompressible flows.

## 6. Results

### 6.1. Gas and Droplet Velocities and Droplet Dispersion

An empirical observation of a gas turbulent round jet is that the profiles of  $\hat{U}$ ,  $\hat{k}$  and  $\hat{\nu}_T$  as function of  $\hat{y}$  becomes self-similar (i.e. independent of the axial coordinate) from some distance to the nozzle exit. Furthermore, there is a linear relation between the half-radius ( $y_{1/2}$ ) and the axial coordinate, that is, the jet sprad rate is constant:

$$S = \frac{dy_{1/2}(x)}{dx}. \quad (22)$$

Chen et al. [9] has experimentally shown that self-similarity also occurred for  $\hat{U}$  in the presence of the spray jet for  $x/D \geq 10$ . For arriving at this

conclusion, it assumed the velocity measured for the smaller droplets ( $D < 3\mu m$ ) as being the gas velocity.

The group of Figures 2 shows the same investigation for the gas velocity field obtained in the numerical simulation. The Figure 2a shows the profiles of  $\hat{U}$  for several axial coordinates. Differently than the experiment, the self-similarity only occurs for  $x/D \geq 15$  (and not for  $x/D \geq 10$ ). This suggests that the transition from the jet developing region to the turbulent region is retarded in the simulation.

Figures 2b and 2c show that the evolution to self-similar profiles is slower for the turbulent quantities  $\hat{k}$  and  $\hat{\nu}_T$  and one may not say that the self-similarity was achieved inside the domain. Chen et al. [9] has shown that for  $x/D \leq 25$  it was also not achieved in the experiment for the root mean square of the axial velocity fluctuation ( $< U_x'' >$ ).

One observation concerning the turbulent viscosity ( $\hat{\nu}_T$ ) is that the centerline value seems to evolve to a value of  $\hat{\nu}_T = 0.047$ , higher than values found in the literature for the turbulent round jet. Pope [26] reports a self-similar turbulent viscosity at centerline of  $\hat{\nu}_T = 0.029$ .

The jet spread rate measures the spread of the axial velocity in the radial direction. A value about  $S = 0.095$  is found on the literature for the pure gas flow Pope [26], and it is independent of Reynolds number. For the spray jet, however, Chen et al. [9] has reported  $S = 0.0665$ . In the simulation it was found a higher value of  $S = 0.071$ , a difference of 23%.

The Figure 3a shows the indeed different half-radius values found in the simulation and the experiment for the same axial coordinates and Figure 3b compares the self-similar profiles of  $\hat{U}_x$  from the simulation and the experi-

ment.

The overestimation of the round jet spread rate with the default coefficients of k-epsilon model has been reported previously by different authors. Luppès [18] has discussed four alternatives to the correction. The modifications consist not only in changing the model coefficients, but also in tuning of boundary conditions.

### 6.2. Gas and Droplet Velocities and Droplet Dispersion

Chen et al. [9] has presented velocity measurements for droplets of four diameter classes in the spray jet:  $D < 5\mu m$ ,  $10\mu m < D < 20\mu m$ ,  $20\mu m < D < 30\mu m$  and  $30\mu m < D < 40\mu m$ . The importance of separating the data in droplet size classes is that the drag force is dependent on its size.

Figure 4 shows in red squares the measured radial profiles of the mean axial velocity for the gas phase ( $\tilde{U}_x$ ) in the axial coordinates of:  $x/D = 5, 10, 15, 20$  and  $25$ . The radial profile obtained in the simulation is also shown in a solid black line. It is evident that the underprediction of the gas velocity in the simulation becomes higher in the downstream direction. In the axial coordinate of  $x/D = 25$ , the centerline value in the simulation is about 20% below the experimental value. In fact, Luppès [18] has reported an error of the same percentual magnitude using the k-epsilon model with the default coefficients.

Chen et al. [9] has also reported the root mean square of the axial and the radial velocities, respectively  $\langle U_x'' \rangle$  and  $\langle U_y'' \rangle$ . Again, the values for the smaller droplets ( $D < 5\mu m$ ) are being used to represent the gas velocity. The same quantities are not provided in the simulation for direct comparison. The turbulence model only solves for the turbulent kinetic energy and its

dissipation rate. A characteristic velocity, however, may be defined as  $\langle U'' \rangle = \sqrt{2/3k}$ . This quantity is shown in Figure 5 with  $\langle U_x'' \rangle$  and  $\langle U_y'' \rangle$ . Again, it is shown radial profiles for different axial coordinates.

Three observations are readily made:

- The radial profile of  $\langle U_x'' \rangle$  is similar to that of  $\langle U_y'' \rangle$ ;
- The characteristic velocity defined for the k-epsilon model ( $\langle U'' \rangle$ ) agrees well with  $\langle U_x'' \rangle$  and  $\langle U_y'' \rangle$ ;
- $\langle U'' \rangle$  declines faster than  $\langle U_x'' \rangle$  and  $\langle U_y'' \rangle$  as the axial coordinate increases.

The first observation indicates that the turbulent jet differs from the self-similar profiles found in the literature Pope [26], where  $\langle U_x'' \rangle$  is about twice as big as  $\langle U_y'' \rangle$  in the centerline. It remains the question whether this occurs because the jet is not fully developed or because of some spray influence.

The second observation suggests that the k-epsilon model is appropriate to describe the round jet turbulence, providing an appropriate characteristic velocity. The third observation, however, indicates that the turbulent dissipation is overpredicted.

Returning to the mentioned influence of the discrepancies in the mean axial velocity of the gas phase on the droplet velocities, the lower velocity of the gas increases the droplet slip velocity and causes a larger drag to be felt by them. The obvious conclusion is that the same discrepancy in the gas velocity will be observed in the comparison of experimental and numerical values for the droplet velocities.

Figure 6 shows in red squares the radial velocity profile measured by Chen et al. [9] for droplets in the class of  $10\mu m < D < 20\mu m$  in the axial coordinates of:  $x/D = 5, 10, 15, 20$  and  $25$ . For each radial position, the velocity value is the ensemble average of the droplets crossing the laser PDI beams. The droplet velocity obtained in the simulation is also shown as black scattered points representing each of them a different droplet in the computation, no averaging was performed.

It is observed that the computed droplet velocity also becomes systematically lower than the measurements in the downstream direction.

### 6.3. Liquid and Vapor Mass Fluxes

The correct prediction of droplet evaporation is, together with the velocity, of high importance for the applications of the spray simulation. The reasonably low discrepancies found for droplet velocity in Figure 6 already indicates that the evaporation model performed well. This is due to the fact that an incorrect modeling of evaporation would lead to an erroneous droplet diameter, further affecting the velocity prediction.

Figure 7 shows the numerical and the experimental liquid mass flow rate for different axial coordinates. The computed values are in good agreement with the measurements for  $x/D \leq 10$ . Further downstream, the simulation overpredicts the liquid flow rate. Clearly, this means that droplet evaporation is lower than it should be. In fact, in Figure 8, it is made the comparison of experimental and numerical radial profiles of vapor mass fluxes and the trend is exactly the same: as the axial coordinate increases, less vapor (hence more liquid) is present in the simulation than it is in the experiment.



The underestimation of evaporation rate has also been noticed in a large-eddy simulation performed by Bini and Jones [7], where it was discussed the effect of a subgrid model to the evaporation. It is said that the lack of a subgrid model affects evaporation mainly in the jet core. In fact, the evaporation model presented in Section 3 only dealt with mean flow properties and transfer coefficients, and the temperature and mass fraction oscillations,  $(T'')$  and  $(Y''_{ac})$ , were not taken into account.

Surely, for a large-eddy simulation, the lack of a subgrid model is less severe than it is in RANS modeling, since at least the non-filtered oscillations are present.

It must also be pointed that uncertainties in the gas mean velocity also affect the prediction of droplet heating and evaporation because of the different slip velocity. The correct attempt to improve accuracy of the present computation would be to adjust the turbulence model to first correct the gas mean velocity and see the new evaporation rates. Next, a stochastic subgrid model for the heat and mass transfer coefficients could be studied.

The last studied property of the spray is the droplet Sauter mean diameter (SMD). Figure 9 shows the numerical and experimental radial profiles of SMD.

The computed Sauter mean diameter shows a good agreement with measurements, in despite of the uncertainty about the droplet size distribution in the boundary conditions and the higher liquid flow rates in Figure 7. This may also be a consequence of the low variance in droplet diameter in the nozzle injection.

This agreement also confirms that the velocity discrepancy is caused by

the anomalous jet spread rate. As discussed previously, if diameters were also in disagreement, the predicted drag force on the droplets would be further incorrect.

## 7. Conclusions

The velocity of both the gas and the liquid phase were underpredicted due to the high turbulent viscosity of the turbulence model. It is suggested in the literature that this discrepancies for a round jet might be diminished by changing the model coefficients and reducing the turbulent length scale in the jet inlet boundary condition.

The evaporation rate was underpredicted after the jet developing region. Turbulence effects on Nusselt and Sherwood numbers were not modeled and this is believed to decrease evaporation, specially in the jet core, as reported by Bini and Jones [7].

Disagreements in the prediction of gas velocity may also have contributed to differences in the evaporation rate. The error in liquid mass flow rate at some axial location was about 20%.

The shape of the radial profile of vapor mass flux was well predicted. The same can be said to the SMD radial profiles.

Future work could explore improvements in the round jet turbulence modeling and new heating and evaporation models for RANS simulations accounting for fluctuations of flow properties.

## References

- [1] S. Aggarwal, F. Peng, Journal of engineering for gas turbines and power 117 (1995).
- [2] A. Amsden, P. O'Rourke, T. Butler, KIVA-II: A Computer Program for Chemically Reactive Flows with Sprays, Technical Report, Los Alamos National Laboratory, 1989.
- [3] S. Apte, K. Mahesh, P. Moin, Proceedings of the Combustion Institute 32 (2009) 2247–2256.
- [4] S. Balachandar, J. Eaton, Annual Review of Fluid Mechanics 42 (2010) 111–133.
- [5] G. Batchelor, An introduction to fluid dynamics, Cambridge Univ Pr, Cambridge, 2000.
- [6] C. Baumgarten, Mixture formation in internal combustion engines, Springer Verlag, Hannover, 2006.
- [7] M. Bini, W. Jones, International Journal of Heat and Fluid Flow 30 (2009) 471–480.
- [8] C. Brennen, Fundamentals of multiphase flow, Cambridge Univ Pr, 2005.
- [9] Y. Chen, S. Stårner, A. Masri, International journal of multiphase flow 32 (2006) 389–412.

- [10] C. Crowe, J. Chung, T. Troutt, Progress in energy and combustion science 14 (1988) 171–194.
- [11] S. De, K. Lakshmisha, R. Bilger, Combustion and Flame 158 (2011) 1992–2008.
- [12] A. Favre, Problems of hydrodynamics and continuum mechanics (1969) 231–266.
- [13] J. Ferziger, M. Perić, Computational methods for fluid dynamics, volume 2, Springer Berlin, 1999.
- [14] R. Issa, Journal of Computational physics 62 (1986) 40–65.
- [15] H. Jasak, Error analysis and estimation for the finite volume method with applications to fluid flows, Ph.D. thesis, Imperial College, London, 1996.
- [16] B. Launder, B. Sharma, Letters Heat Mass Transfer 1 (1974) 131–137.
- [17] H. Liu, Science and engineering of droplets: fundamentals and applications, William Andrew, 2000.
- [18] R. Luppés, The numerical simulation of turbulent jets and diffusion flames, Ph.D. thesis, Technische Universiteit Eindhoven, Eindhoven, 2000.
- [19] G. Macpherson, N. Nordin, H. Weller, Communications in Numerical Methods in Engineering 25 (2009) 263–273.

- [20] A. Majda, J. Sethian, Combustion science and technology 42 (1985) 185–205.
- [21] B. Muller, Lecture series - van Kareman Institute for fluid dynamics 3 (1999) E1–E51.
- [22] P. Nordin, Complex chemistry modeling of diesel spray combustion, Ph.D. thesis, Chalmers University of Technology, Goteborg, 2001.
- [23] OpenCFD, OpenFOAM’s Programmers Guide, OpenCFD Limited, London, 2008.
- [24] P. O’Rourke, Journal of Computational Physics 83 (1989) 345–360.
- [25] T. Poinso, D. Veynante, Theoretical and numerical combustion, RT Edwards, Inc., 2005.
- [26] S. Pope, Turbulent flows, Cambridge Univ Pr, 2000.
- [27] W. Ranz, W. Marshall, Chem. Eng. Prog 48 (1952) 141–146.
- [28] J. Reveillon, L. Vervisch, in: Proceedings of the Summer Program, pp. 25–38.
- [29] W. Sirignano, C. Edwards, Journal of Fluids Engineering 122 (2000) 189.
- [30] M. Sommerfeld, Theoretical and Experimental Modelling of. Particulate Flows., Von Karman Institute for Fluid Dynamics., 2000.

- [31] C. Viozat, Implicit Upwind Schemes for Low Mach Number Compressible Flows, Technical Report RR-3084, INRIA, SINUS - INRIA Sophia Antipolis - INRIA, 1997.
- [32] M. Wakil, O. Uyehara, P. Myers, A theoretical investigation of the heating-up period of injected fuel droplets vaporizing in air, Technical Report, Wiscosin Univ-Madison, Wiscosin Univ-Madison, 1954.
- [33] H. Weller, G. Tabor, H. Jasak, C. Fureby, Computers in physics 12 (1998) 620.
- [34] D. Wilcox, La Canada, CA: DCW Industries, Inc, 1993. (1993).

## List of Figures

1	Configuration of the spray jet nozzle of Chen et al. [9]. . . . .	25
2	Numerical results showing the evolution to self-similar profiles of the following gas phase properties: (a) dimensionless mean axial velocity - $\hat{U}_x$ , (b) dimensionless turbulent kinetic energy - $\hat{k}$ - and (c) dimensionless turbulent viscosity - $\hat{\nu}_t$ . The different curves show the profiles for the correspondent axial coordinate indicated in the legend. . . . .	26
3	(a) Half-radius as a function of the axial coordinate in the experiment and in the simulation. (b) Self-similar radial profile of the numerical and the experimental dimensionless axial velocity - $\hat{U}_x$ . The measurements were obtained from Chen et al. [9]. . . . .	27
4	Measured and computed radial profiles of the mean axial velocity of the gas phase ( $\tilde{U}_x$ ). The measurements were obtained from Chen et al. [9]. . . . .	28
5	Measured radial profiles of the gas phase velocities $\langle U_x'' \rangle$ and $\langle U_y'' \rangle$ and the characteristic velocity defined for the k-epsilon model $\langle U'' \rangle = \sqrt{2/3k}$ obtained from the simulation. The measurements were obtained from Chen et al. [9]. . . . .	29
6	Red squares are the measured radial profile of the mean axial velocity of droplets ( $\tilde{U}_{d,x}$ ) in the size class of $10\mu m < D < 20\mu m$ . Scattered black dots are the computed velocities for each droplet in the numerical simulation. The measurements were obtained from Chen et al. [9]. . . . .	30

7	Droplet mass flow rate at four axial locations. The measurements were obtained from Chen et al. [9]. . . . .	31
8	Radial profiles of mean axial mass flux of acetone vapor: $\dot{m}''_{ac} = \rho \bar{Y}_{ac} \tilde{U}_x$ . The measurements were obtained from Chen et al. [9].	32
9	Numerical and experimental radial profiles of Sauter mean diameter (SMD). The measurements were obtained from Chen et al. [9]. . . . .	33



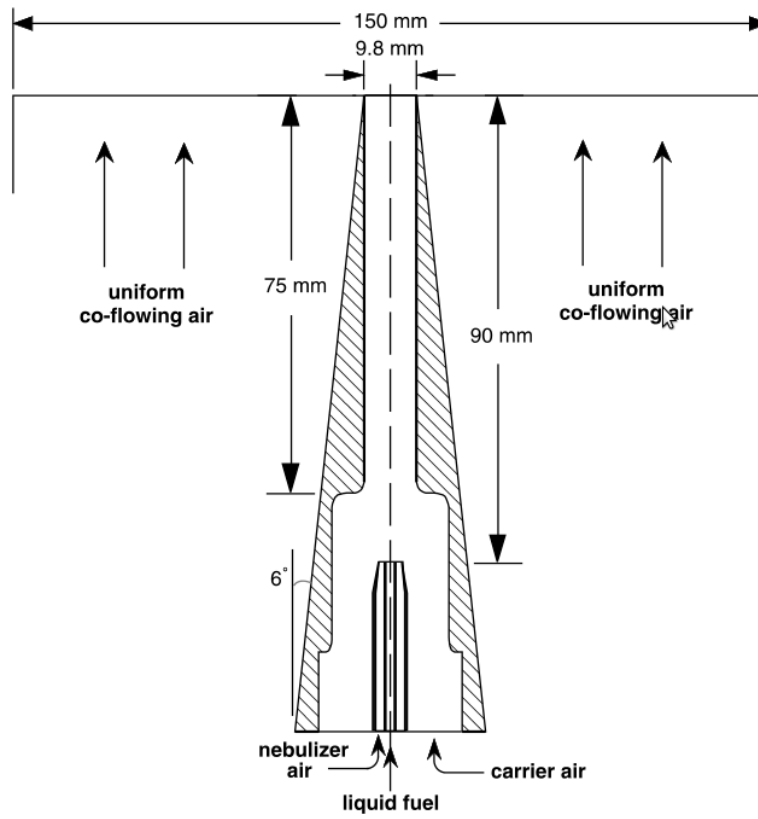


Figure 1: Configuration of the spray jet nozzle of Chen et al. [9].

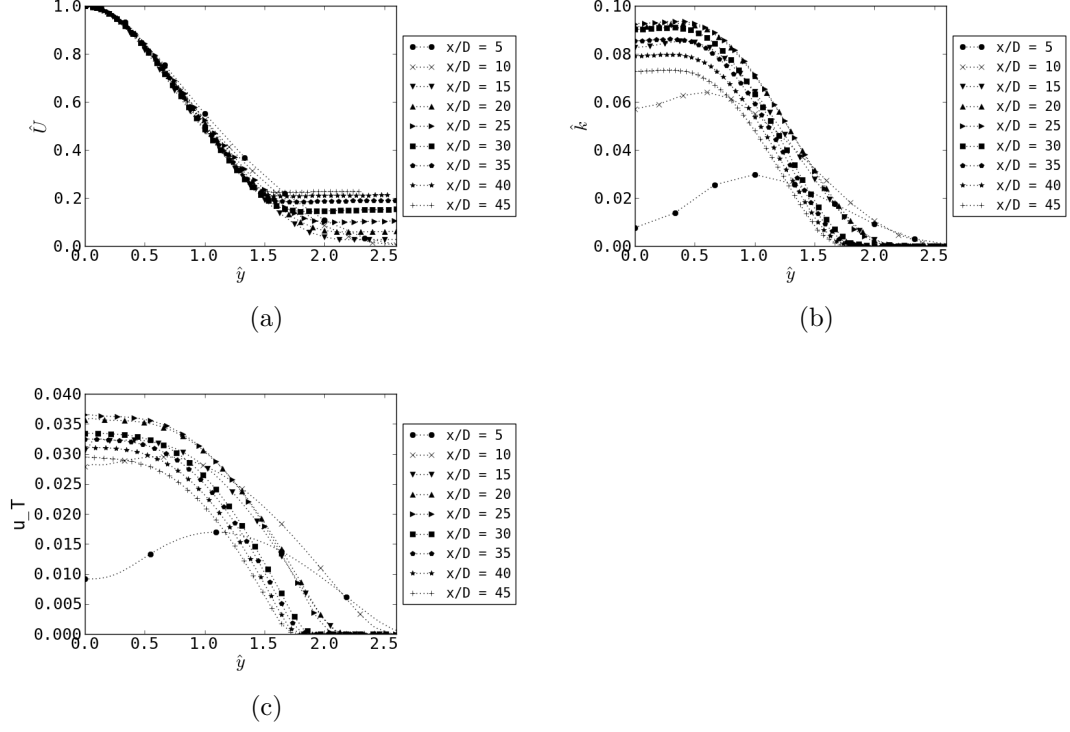
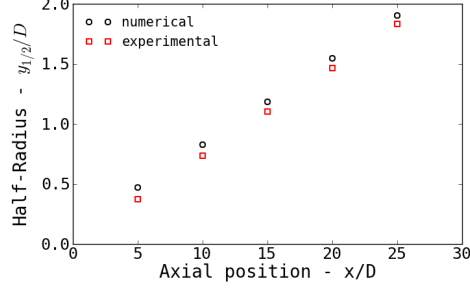
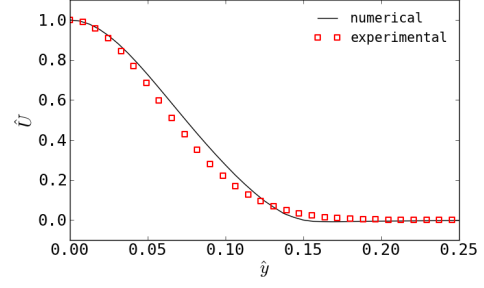


Figure 2: Numerical results showing the evolution to self-similar profiles of the following gas phase properties: (a) dimensionless mean axial velocity -  $\hat{U}_x$ , (b) dimensionless turbulent kinetic energy -  $\hat{k}$  - and (c) dimensionless turbulent viscosity -  $\hat{\nu}_t$ . The different curves show the profiles for the correspondent axial coordinate indicated in the legend.

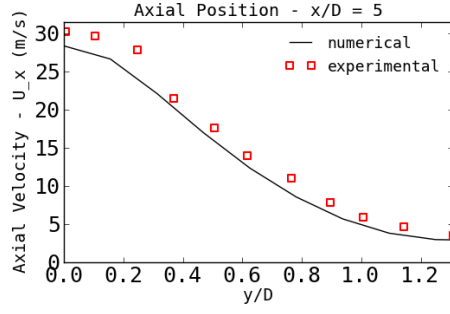


(a)

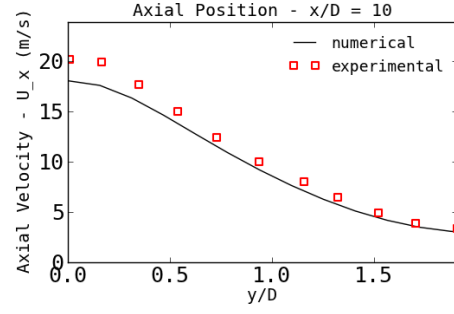


(b)

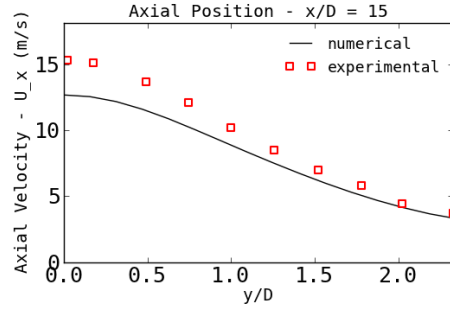
Figure 3: (a) Half-radius as a function of the axial coordinate in the experiment and in the simulation. (b) Self-similar radial profile of the numerical and the experimental dimensionless axial velocity -  $\hat{U}_x$ . The measurements were obtained from Chen et al. [9].



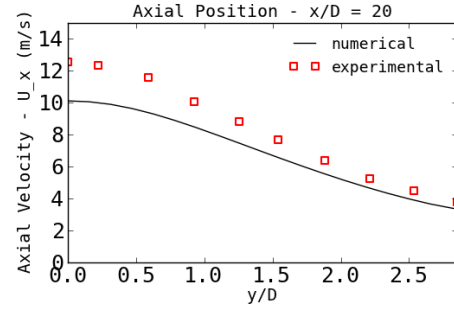
(a)



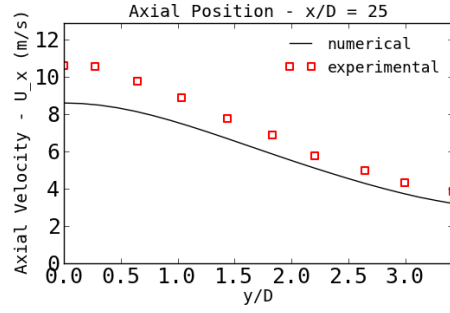
(b)



(c)

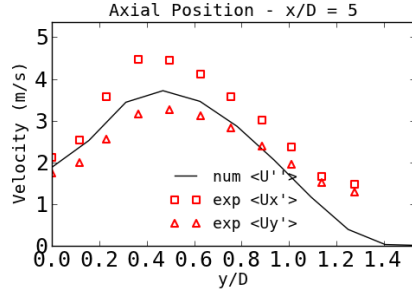


(d)

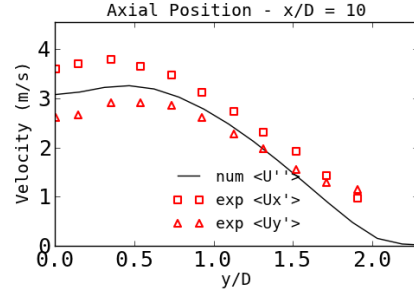


(e)

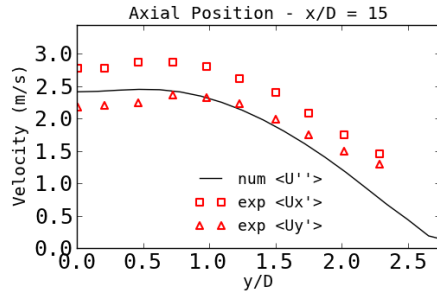
Figure 4: Measured and computed radial profiles of the mean axial velocity of the gas phase ( $\bar{U}_x$ ). The measurements were obtained from Chen et al. [9].



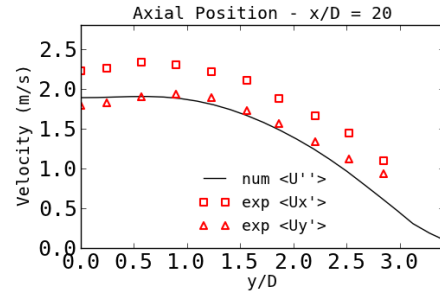
(a)



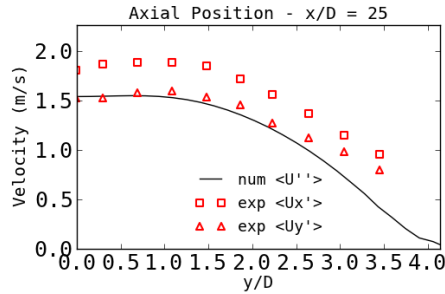
(b)



(c)



(d)



(e)

Figure 5: Measured radial profiles of the gas phase velocities  $\langle U_x'' \rangle$  and  $\langle U_y'' \rangle$  and the characteristic velocity defined for the k-epsilon model  $\langle U'' \rangle = \sqrt{2/3k}$  obtained from the simulation. The measurements were obtained from Chen et al. [9].

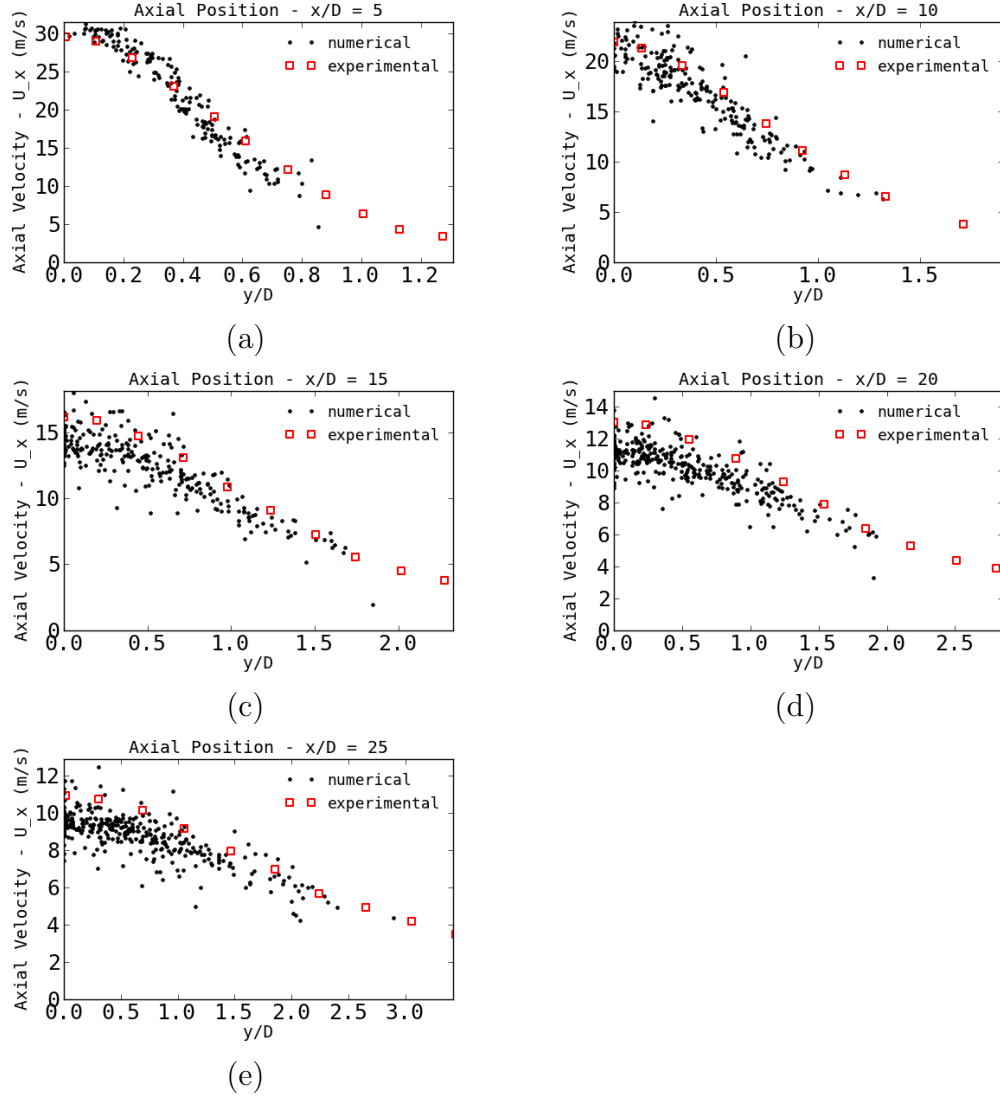


Figure 6: Red squares are the measured radial profile of the mean axial velocity of droplets ( $\tilde{U}_{d,x}$ ) in the size class of  $10\mu m < D < 20\mu m$ . Scattered black dots are the computed velocities for each droplet in the numerical simulation. The measurements were obtained from Chen et al. [9].

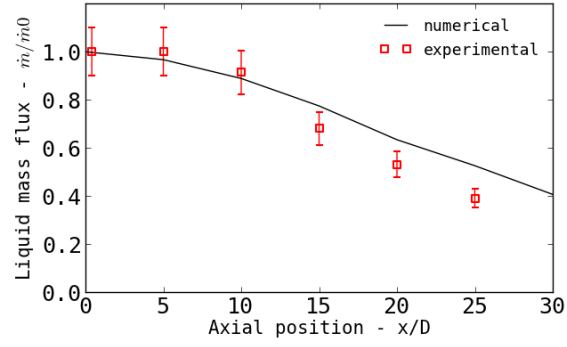


Figure 7: Droplet mass flow rate at four axial locations. The measurements were obtained from Chen et al. [9].

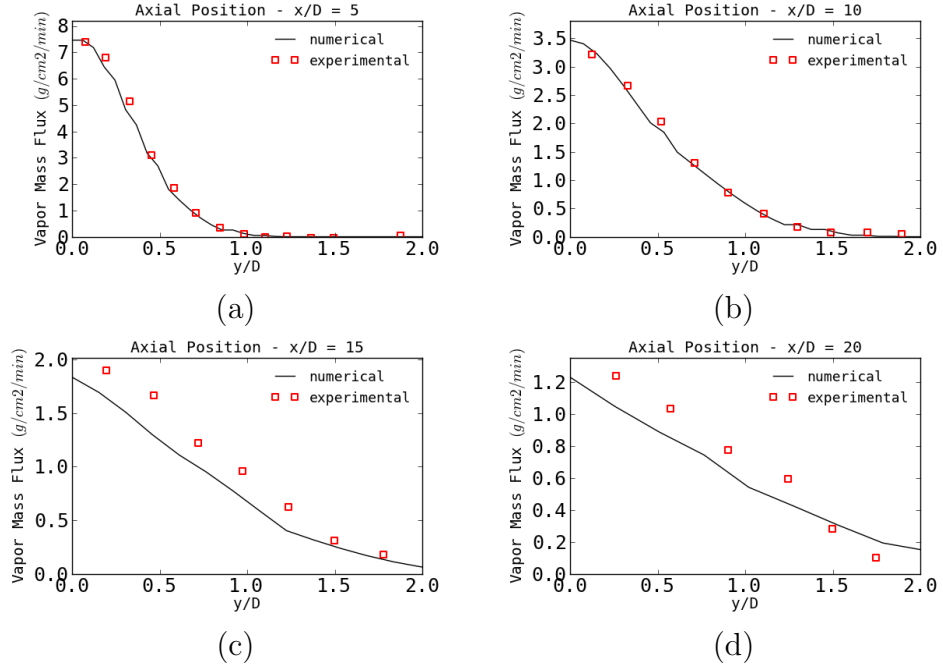
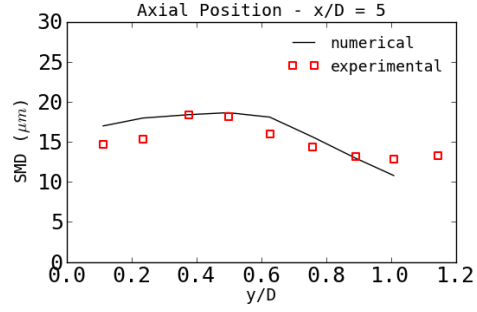
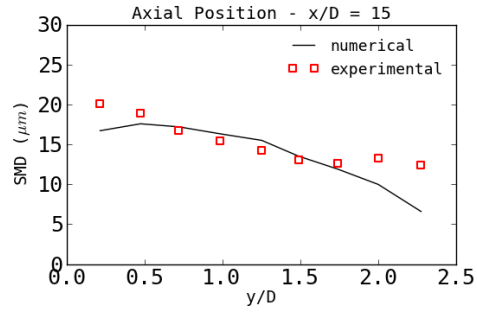


Figure 8: Radial profiles of mean axial mass flux of acetone vapor:  $\dot{m}''_{ac} = \rho \bar{Y}_{ac} \bar{U}_x$ . The measurements were obtained from Chen et al. [9].

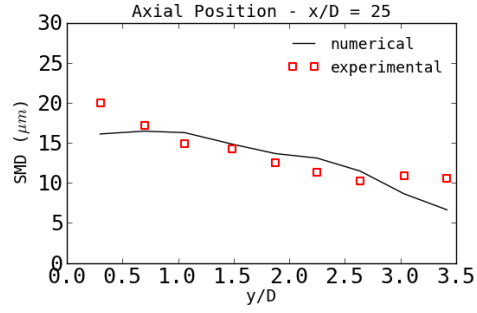




(a)



(b)



(c)

Figure 9: Numerical and experimental radial profiles of Sauter mean diameter (SMD). The measurements were obtained from Chen et al. [9].

## List of Tables

1	Basic information about the experiment of Chen et al. [9]. . .	35
2	k-epsilon model constants. . . . .	36

Experiment Data	
Liquid Phase	Acetone
Liquid Flow rate at nozzle exit ( $g/min$ )	7.0
Carrier air flow rate ( $g/min$ )	135
Vapor flux at nozzle exit ( $g/min$ )	5.0
SMD at nozzle exit ( $\mu m$ )	13.7
Gas temperature at nozzle exit ( $K$ )	280
Gas jet Reynolds Number ( $Re = 4\dot{m}_g/\pi D_{nozzle}\mu_g$ )	16,300

Table 1: Basic information about the experiment of Chen et al. [9].

$C_\mu$	0.09
$C_{\epsilon 1}$	1.44
$C_{\epsilon 2}$	1.92
$C_{\epsilon 3}$	-0.33
$\sigma_k$	1
$\sigma_\epsilon$	1.3

Table 2: k-epsilon model constants.